Supplementary Information

Seasonal and regional sensitivities of secondary inorganic aerosols to NH_3 and NO_x emission reductions over China

Jiayu Xu[1], Alain Clappier[2*], Philippe Thunis[3], Xingpei Ye[4], Lu Li[1], and Lin Zhang[1*]

[1]Peking University, School of Physics, Department of Atmospheric and Oceanic Sciences, Beijing, China

[2]Université de Strasbourg, Laboratoire Image Ville Environnement, Strasbourg, France

[3]European Commission, Joint Research Centre (JRC), Ispra, Italy

[4]Jiangsu Guoxin Research Institute Co., Ltd., Nanjing, China

Correspondence to: Alain Clappier (alain.clappier@live-cnrs.unistra.fr) and Lin Zhang (zhanglg@pku.edu.cn)

This file includes:

Supplementary Text S1

Supplementary Figures S1 – S12

Supplementary Tables S1

Text S1. Methods for assessing health effects associated with $PM_{2.5}$ exposure

S1.1 Population-weighted concentration

The population-weighted concentration (PWC) is calculated by weighting pollutant concentrations with the population exposed at different concentration levels, reflecting the overall impact of pollutant exposure under a normalized population distribution. The calculation follows Equation S1:

$$\mathrm{PWC} = \frac{\sum_{i=1}^{n}(P_i \times C_i)}{P} \tag{S1}$$

where n is the total number of grid cells within the study region and i represents an individual grid therein; P_i and C_i denote the population and pollutant's mean concentration in grid i, respectively; P is the total population within the study region.

The gridded population data used in this study are derived from the LandScan Global 2017 dataset (https://landscan.ornl.gov/), which estimates global population distribution by integrating geographic information science, remote sensing techniques, and machine learning algorithms. With a spatial resolution of 30 arcseconds (~1 km), LandScan provides the highest-resolution global population dataset and is recognized as the community standard for population distribution. The total population for each province of China is constrained using 2017 statistical data from the China Statistical Yearbook (http://www.stats.gov.cn/tjsj/ndsj/).

S1.2 $PM_{2.5}$-related and SNA-attributable premature deaths

The quantitative estimate of attributable mortality due to ambient fine particulate matter ($PM_{2.5}$) exposure is primarily based on disease-specific relative risk models. Following the method in Zhou et al. (2021) and Liu et al. (2023), this study employs the Global Exposure Mortality Model (GEMM) to assess the mortality associated with $PM_{2.5}$ exposure. The GEMM model focuses on non-accidental mortality (Burnett et al., 2018), the vast majority (>99%) of which results from noncommunicable diseases (NCDs, including ischemic heart disease, stroke, chronic obstructive pulmonary disease, and lung cancer), as well as lower respiratory infections (LRIs). Therefore, this study restricts the estimation of premature mortality to these two disease subgroups.

The estimation of premature mortality due to $PM_{2.5}$ exposure is typically based on a log-linear model (EPA, 2014). The GEMM model develops a log-nonlinear hazard ratio (HR) function as follow to characterize the age-specific association between $PM_{2.5}$ exposure and health risks of NCDs and LRIs:

$$HR_i(z) = exp\left(\theta \times \frac{log\left(1+\frac{z}{\alpha}\right)}{1+exp\left(-\frac{z-\mu}{\vartheta}\right)}\right), \mathrm{z} = \max(0, C_{PM2.5} - 2.4\ \mu\mathrm{g}/m^3) \tag{S2}$$

where i is a certain age group; z represents the $PM_{2.5}$ exposure level, considering health impacts only when the annual mean surface $PM_{2.5}$ concentration ($C_{PM2.5}$) is larger than 2.4 μg m^{-3}; *exp* denotes the natural exponential function, and *log* refers to the natural logarithm function; α, μ, and v are the parameters determining the shape of HR function, with age-specific values derived from Burnett et al. (2018); θ is the concentration-response factor. In this study, the population affected by $PM_{2.5}$ exposure is categorized into 12 age groups: five-year intervals from 25 to 79 years, with 80+ as one group. Additionally, we assume θ follows a normal distribution, with the uncertainty range provided by Burnett et al. (2018), and perturb the value of θ 100,000 times using the Monte Carlo approach to account for the uncertainty in the HR estimate. As a result, a range of values and 95% confidence intervals for $HR_i(z)$ are obtained.

On the basis of HR, the $PM_{2.5}$-related premature mortality (ΔMort) for adults (aged ≥ 25) is calculated by the following formula:

$$\Delta\mathrm{Mort} = \sum_i Mort_{0i} \times \frac{HR_i - 1}{HR_i} \times Pop_i \tag{S3}$$

where Mort_{0i} is the baseline mortality rate of NCDs and LRIs for age group i, provided by the Global Burden of Disease (GBD) study (https://vizhub.healthdata.org/gbd-results/). Pop_i is the statistical population of age group i, from the China Statistical Yearbook (http://www.stats.gov.cn/tjsj/ndsj/).

Since the GEMM HR function is log-nonlinear in total $PM_{2.5}$ concentrations, it is not separable across chemical components. To isolate the premature deaths attributable to SNA, we therefore adopt an attribution-by-difference approach. First, a total $PM_{2.5}$-related premature mortality is calculated from the total $PM_{2.5}$ field. Then, the mortality from a counterfactual field in which the SNA concentrations are removed while the exposure remains anchored to total $PM_{2.5}$ is recomputed. The SNA-attributable premature mortality ($\Delta\mathrm{Mort}_{SNA}$) is taken as the difference between the two:

$$\Delta\mathrm{Mort}_{SNA} = \Delta\mathrm{Mort}(C_{PM2.5}) - \Delta\mathrm{Mort}(C_{PM2.5} - C_{SNA}) \tag{S4}$$

where C_{SNA} is the SNA concentration, and the exposure level is estimated as z = max(0, ($C_{PM2.5}$ -C_{SNA}) – 2.4 μg m^{-3}). We note that GEMM was developed from cohort exposure to total $PM_{2.5}$ and assumes that toxicity per unit mass is independent of chemical composition (Burnett et al., 2018). Accordingly, $\Delta\mathrm{Mort}_{SNA}$ reported here represents a mass-based partition of total $PM_{2.5}$ mortality attributable to the SNA fraction, rather than a chemically specific estimate of SNA toxicity.

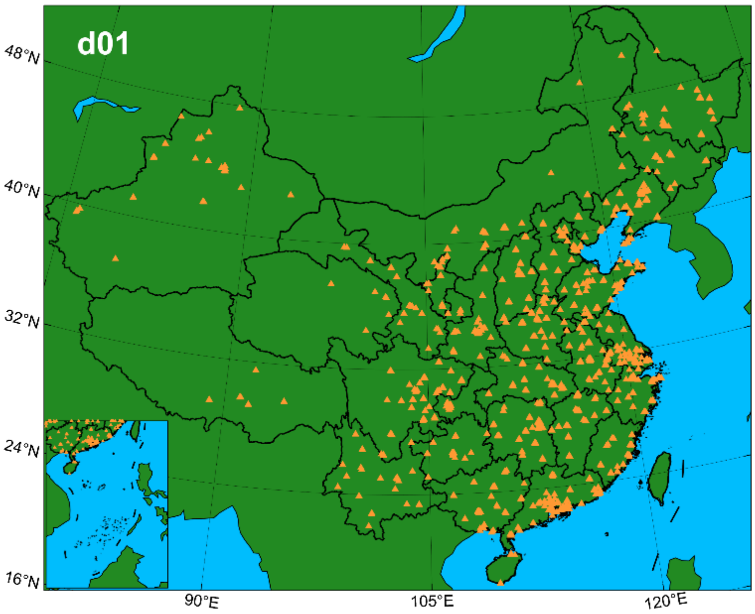

Figure S1. WRF-Chem model grid setup and distribution of CNEMC national urban air quality monitoring stations screened by quality control (orange triangles).

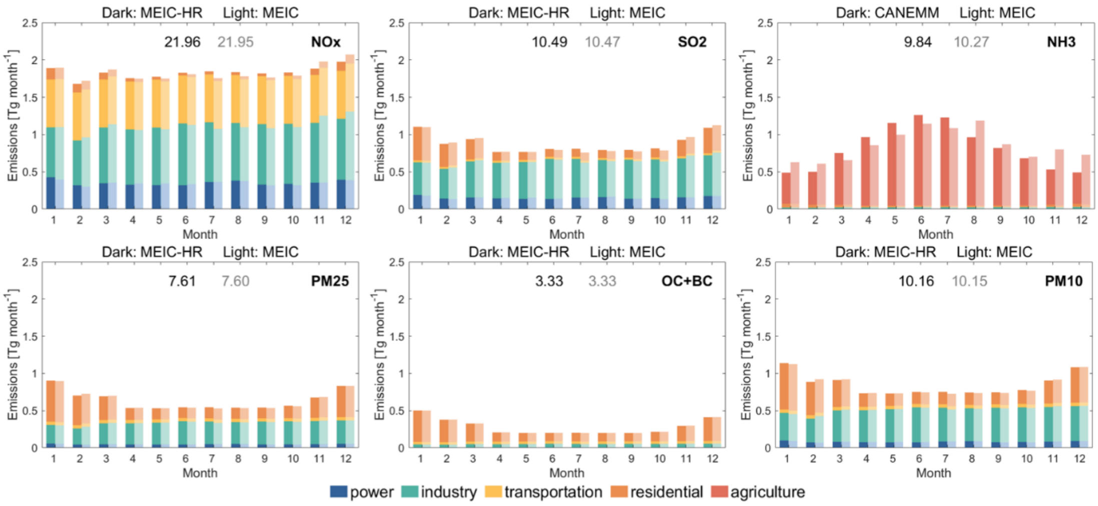

Figure S2. Monthly emissions of NO_x, SO_2, NH_3, $PM_{2.5}$, OC+BC, and PM_{10} in 2017 from the MEIC-HR emission inventory (columns in dark colors; agricultural NH_3 emissions are estimated using the methods of Chen et al. (2021)) and the MEIC emission inventory (columns in light colors). Black and gray numbers represent annually total emissions (Tg year^{-1}) for the dark and light columns, respectively.

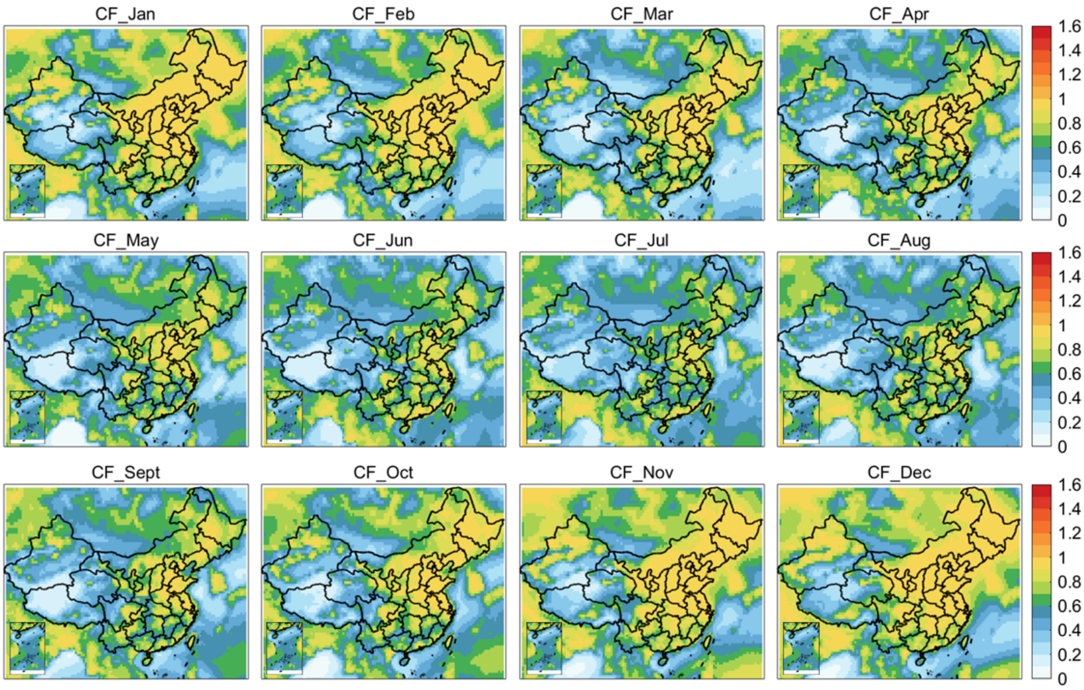

Figure S3. The spatial distributions of monthly corrected factors (CF) for NO_2 observations from January to December, 2017.

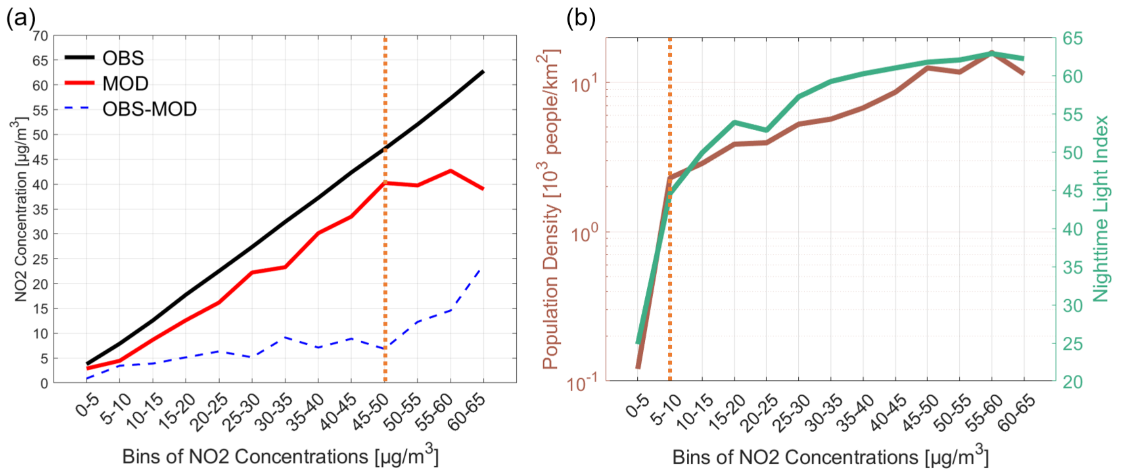

Figure S4. (a) Observed (black) and Base simulated (red) annual mean surface NO_2 concentrations and their differences (blue dash line) in 5 μg m^{-3} intervals. (b) Average population density (brown) and nighttime light indices (green) for observation stations within each 5 μg m^{-3} NO_2 observation bin.

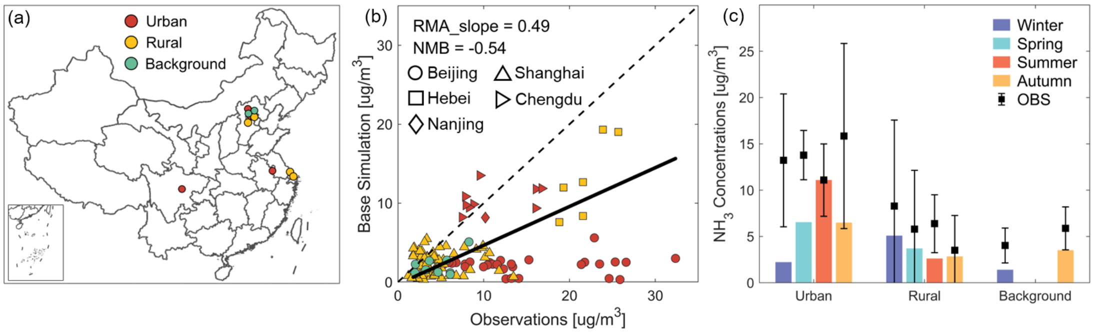

Figure S5. The comparison of surface NH_3 concentrations between the Base simulation and the ground-based observations in 2017. (a) Locations and categories of the NH_3 measurement stations collected in Table S1. (b) Scatter plot comparing simulated and observed NH_3 concentrations, with the solid line indicating Reduced Major Axis (RMA) regression of markers, and the dashed line indicating 1:1; the shapes of markers represent different cities; the marker colors corresponding to the same meaning as in (a); NMB is the Normalized Mean Bias of simulation. (c) Simulated (bar) and observed (black dot with error bar) NH_3 concentrations over 3 land types in four seasons.

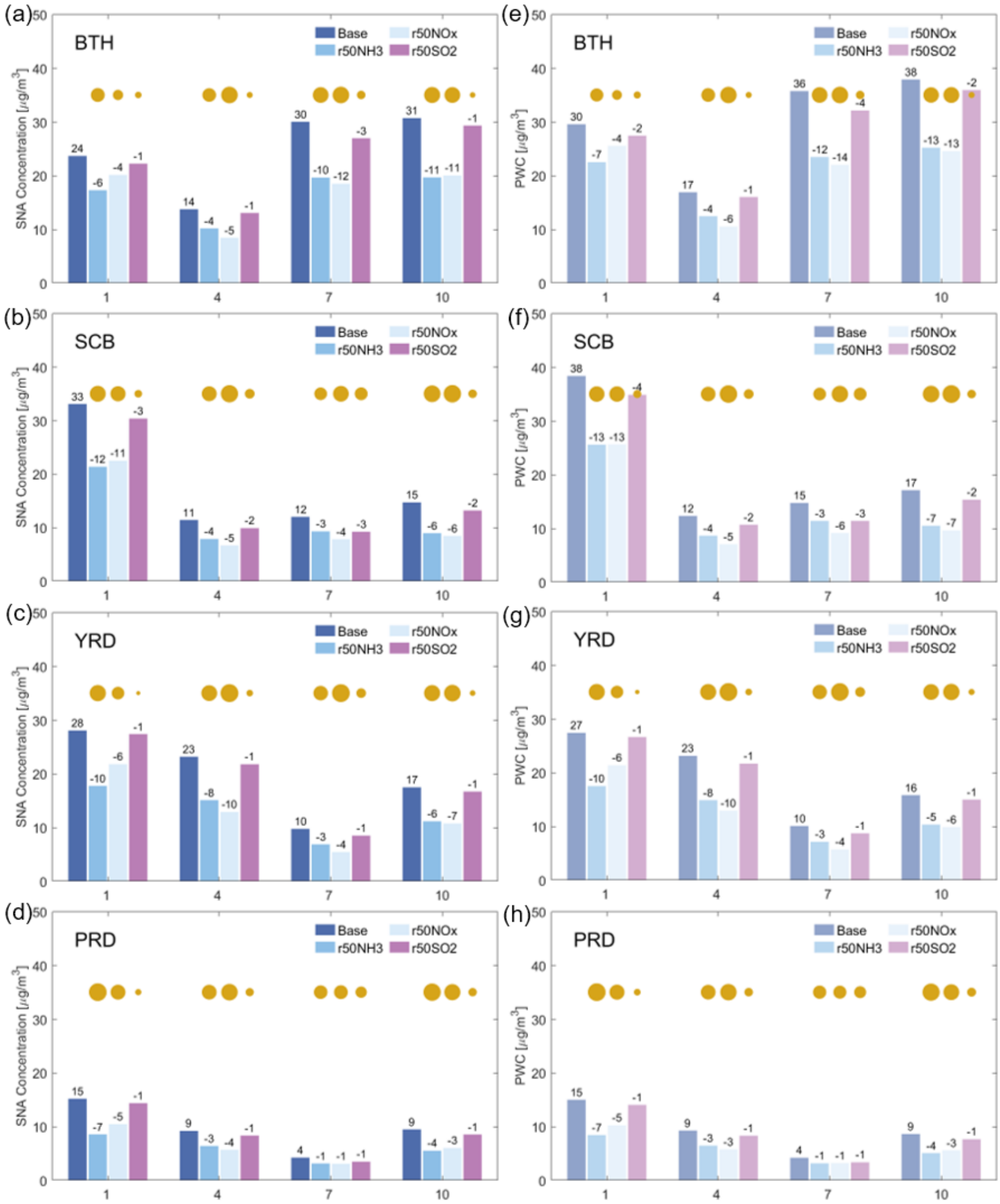

Figure S6. Monthly mean SNA concentrations (μg m^{-3}; a-d) and corresponding population-weighted concentrations (PWC; μg m^{-3}; e-h) in January, April, July, and October in the BTH, SCB, YRD, and PRD regions in Base and precursor abatement scenarios. Numbers above the dark blue columns are monthly means of Base simulation; numbers above the columns in other colors are differences between abatement scenarios and Base case. The areas of the yellow circles indicate the relative reduction percentages in surface SNA or PWC concentrations for abatement scenarios.

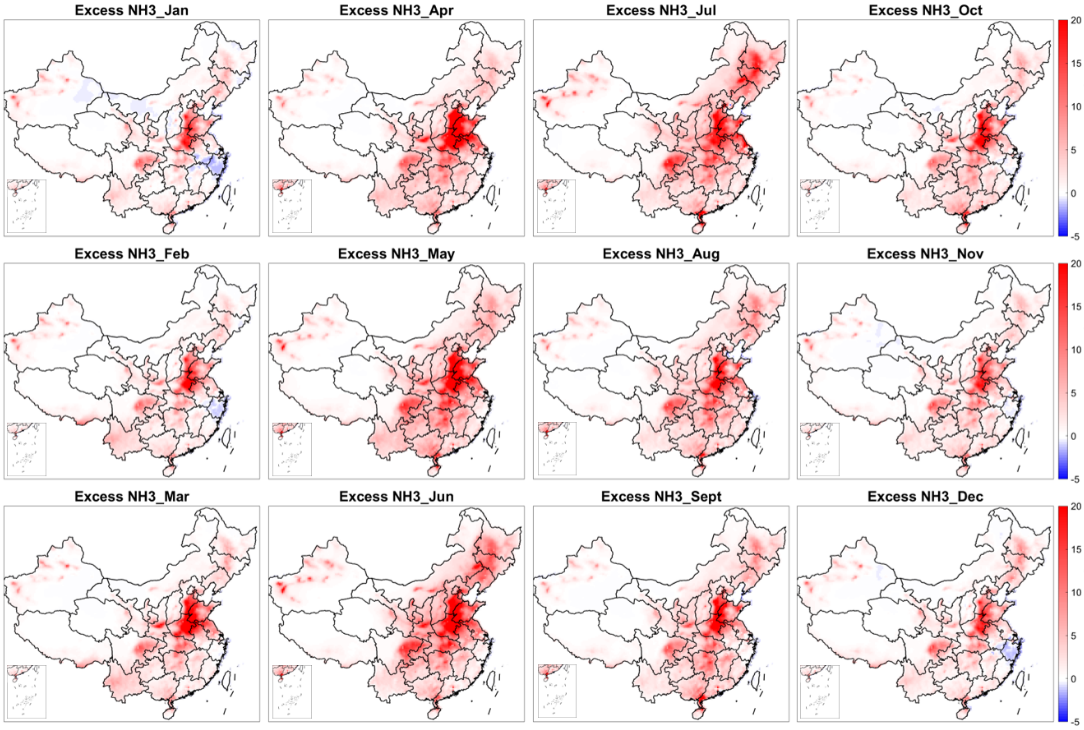

Figure S7. The spatial distributions of the excess NH_3 concentrations (μg m^{-3}) in China from January to December, 2017. The calculation method of excess NH_3 refers to Liu et al. (2021).

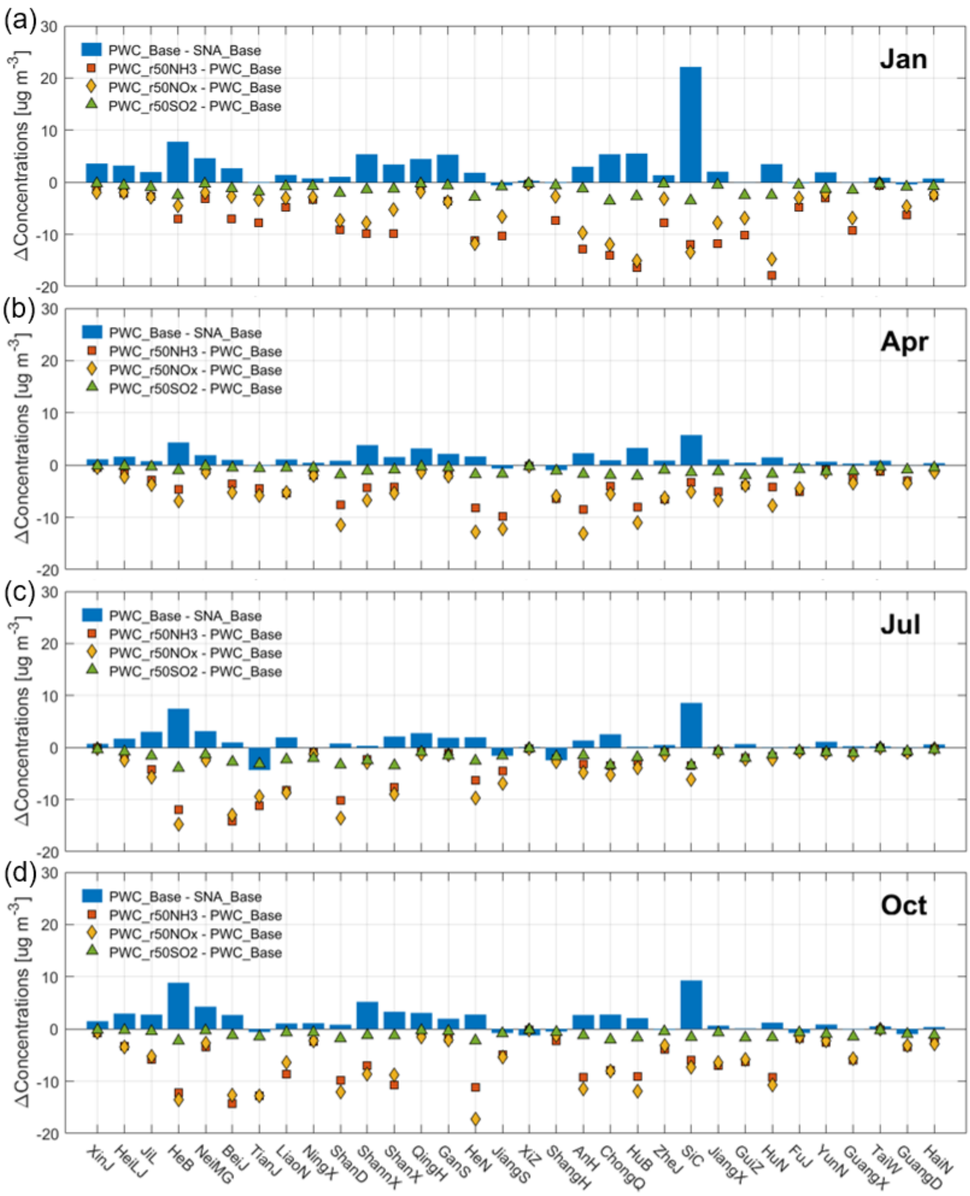

Figure S8. The differences between PWC and absolute concentrations of SNA (μg m^{-3}) in Base simulation (blue columns) for 32 provinces in January (a), April (b), July (c), and October (d), as well as the differences in PWC between each abatement scenario (red squares for r50NH3, yellow diamonds for r50NOx, and green triangles for r50SO2) and Base simulation.

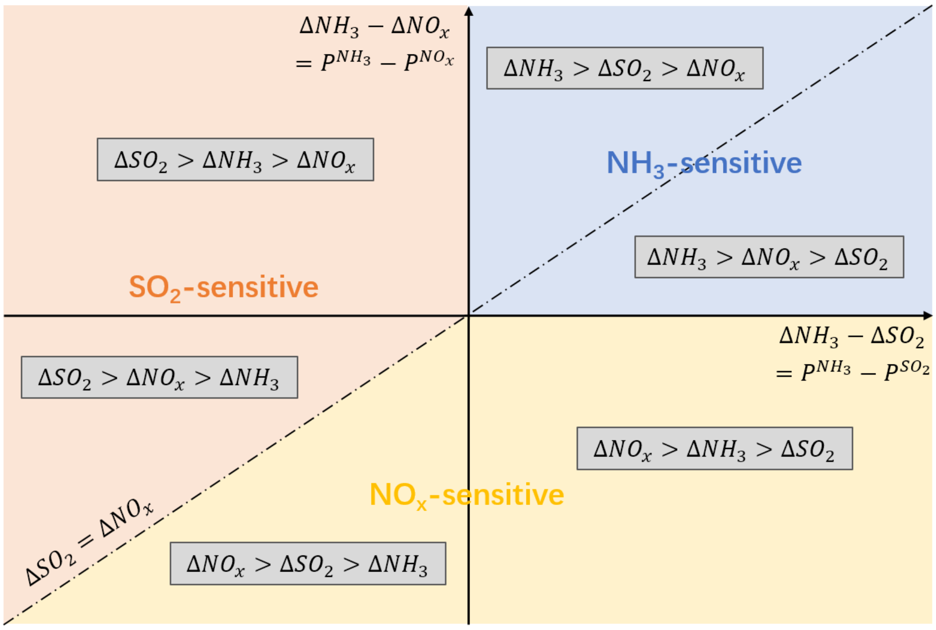

Figure S9. Sensitivity coordinate system of SNA formation chemical regimes. The X-axis denotes the difference between P^{NH3} and P^{SO2}. The Y-axis denotes the difference between P^{NH3} and P^{NOx}. The first quadrant indicates the NH_3-sensitive chemical regime; the second and upper left of the third quadrants indicate the SO_2-sensitive chemical regime; the fourth and lower right of the third quadrants indicate the NO_x-sensitive chemical regime. The dashed 1:1 line denotes the situation of $P^{SO2} = P^{NOx}$.

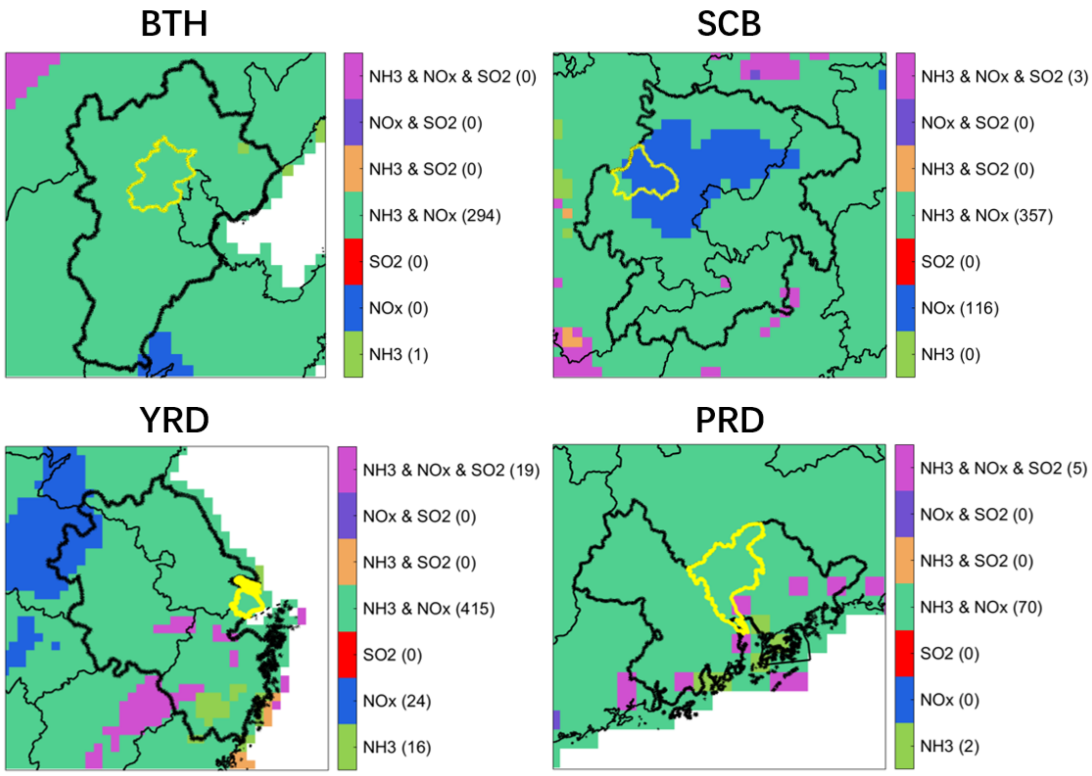

Figure S10. Enlarged view of Fig. 8, providing a more detailed annual variation patterns of SNA formation chemical regimes in the BTH, SCB, YRD, and PRD regions bordered by bold black lines. The Beijing, Chengdu, Shanghai, and Guangzhou are outlined with yellow lines.

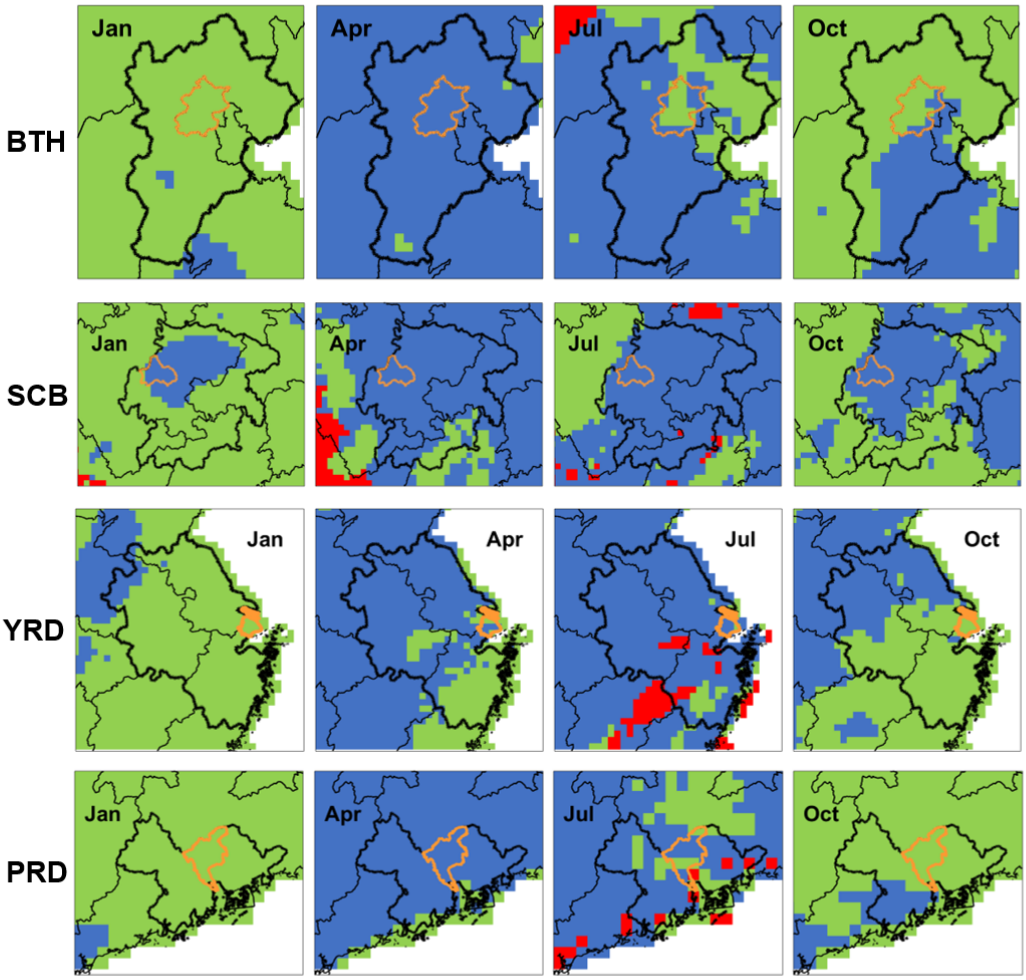

Figure S11. Enlarged view of Fig. 6, providing a more detailed distribution of SNA formation chemical regimes in the BTH, SCB, YRD, and PRD regions bordered by bold black lines. The Beijing, Chengdu, Shanghai, and Guangzhou are outlined with orange lines.

120

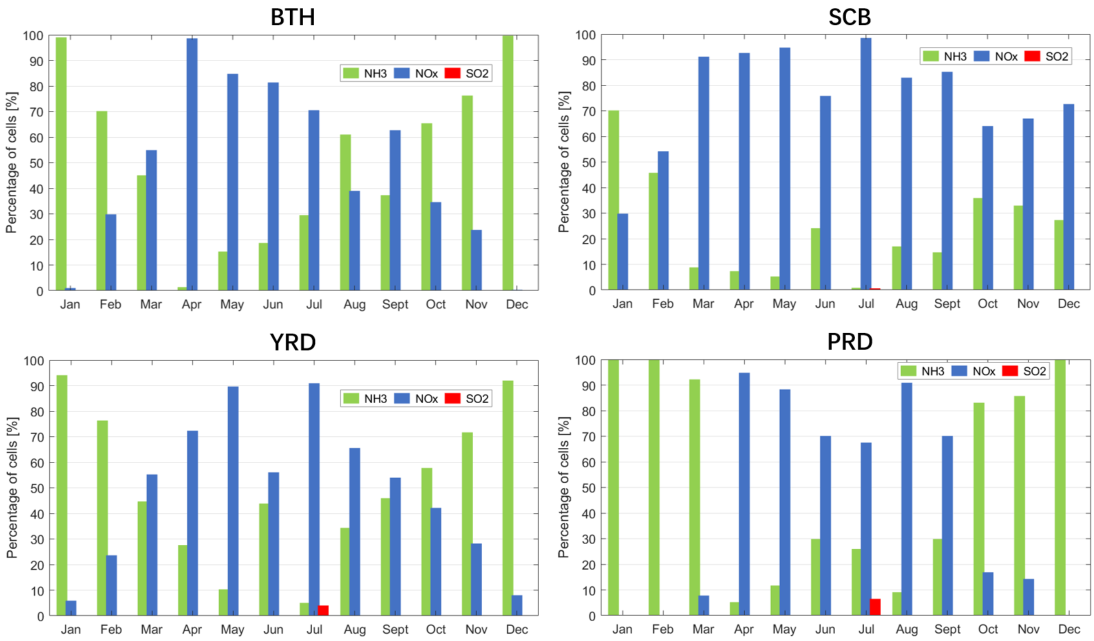

Figure S12. The proportion of grids sensitive to NH_3 emissions (green), NO_x emissions (blue), and SO_2 emissions (red) among all grids within the BTH, SCB, YRD, and PRD regions.

Table S1. Information of NH_3 observational stations collected by this study over China in 2017.

Station name[a]	Lon, Lat	Land-use type	Observation session	Data type[b]	Reference
IAP	116.37°E, 39.97°N	Urban	Jan. 03 - Mar. 16	WA	(Zhang et al., 2018)
CAMS	116.40°E, 39.93°N	Urban	Sept. 01 - Dec. 31	MA	(Pu et al., 2020)
CAU	116.27°E, 40.02°N	Urban	Dec. 27 - Jan. 31	WA	(Zhang et al., 2021)
R3	116.37°E, 39.97°N	Traffic	Dec. 27 - Jan. 31	WA	(Zhang et al., 2021)
R5	116.39°E, 40.02°N	Traffic	Dec. 27 - Jan. 31	WA	(Zhang et al., 2021)
BTin	116.00°E, 41.00°N	Traffic	Dec. 27 - Jan. 31	WA	(Zhang et al., 2021)
BTout	116.00°E, 40.36°N	Background	Dec. 27 - Jan. 31	WA	(Zhang et al., 2021)
SDZ	117.12°E, 40.65°N	Background	Sept. 01 - Dec. 31	MA	(Pu et al., 2020)
XH	116.96°E, 39.75°N	Rural	Nov. 01 - Nov. 30	MA	(Wang, 2021)
GC	115.73°E, 39.15°N	Rural	Jan. 01 - May 31	MA	(Kuang et al., 2020)
CM	121.48°E, 31.68°N	Rural	Mar. 01 - Dec. 31	WA	(Kuang et al., 2022)
SY	121.88°E, 30.99°N	Rural	Mar. 01 - Dec. 31	WA	(Kuang et al., 2022)
NJU	118.72°E, 32.21°N	Urban	Jul. 01 - Aug. 31	MA	(Kuang et al., 2022)
CD	104.06°E, 30.70°N	Urban	Apr. 01 - Dec. 31	MA	(Huang et al., 2021)

a. The abbreviations from top to bottom represent for the Institute of Atmospheric Physics (IAP), Chinese Academy of Meteorological Sciences (CAMS), China Agricultural University (CAU), the 3^{rd} Ring Road (R3), the 5^{th} Ring Road (R5), Badaling Tunnel inside (BTin), Badaling Tunnel outside (BTout), and Shang Dian Zi (SDZ) stations in **Beijing**, Xiang He (XH) and Gu Cheng (GC) stations in **Hebei** Province, Chong Ming (CM) and Shu Yuan (SY) stations in **Shanghai**, Nanjing University (NJU) station in **Jiangsu** Province, and Cheng Du (CD) station in **Sichuan** Province.

b. WA means weekly-average; MA means monthly-average.

References

Burnett, R., Chen, H., Szyszkowicz, M., Fann, N., Hubbell, B., Pope, C. A., Apte, J. S., Brauer, M., Cohen, A., Weichenthal, S., Coggins, J., Di, Q., Brunekreef, B., Frostad, J., Lim, S. S., Kan, H., Walker, K. D., Thurston, G. D., Hayes, R. B., Lim, C. C., Turner, M. C., Jerrett, M., Krewski, D., Gapstur, S. M., Diver, W. R., Ostro, B., Goldberg, D., Crouse, D. L., Martin, R. V., Peters, P., Pinault, L., Tjepkema, M., Van Donkelaar, A., Villeneuve, P. J., Miller, A. B., Yin, P., Zhou, M., Wang, L., Janssen, N. A. H., Marra, M., Atkinson, R. W., Tsang, H., Quoc Thach, T., Cannon, J. B., Allen, R. T., Hart, J. E., Laden, F., Cesaroni, G., Forastiere, F., Weinmayr, G., Jaensch, A., Nagel, G., Concin, H., and Spadaro, J. V.: Global estimates of mortality associated with long-term exposure to outdoor fine particulate matter, Proc. Natl. Acad. Sci. U.S.A., 115, 9592–9597, https://doi.org/10.1073/pnas.1803222115, 2018.

EPA, O.: Environmental Benefits Mapping and Analysis Program - Community Edition (BenMAP-CE), 2014.

Huang, X., Zhang, J., Zhang, W., Tang, G., and Wang, Y.: Atmospheric ammonia and its effect on PM2.5 pollution in urban Chengdu, Sichuan Basin, China, Environmental Pollution, 291, 118195, https://doi.org/10.1016/j.envpol.2021.118195, 2021.

Kuang, Y., Xu, W., Lin, W., Meng, Z., Zhao, H., Ren, S., Zhang, G., Liang, L., and Xu, X.: Explosive morning growth phenomena of NH3 on the North China Plain: Causes and potential impacts on aerosol formation, Environmental Pollution, 257, 113621, https://doi.org/10.1016/j.envpol.2019.113621, 2020.

Kuang, Y., Chang, Y., Cheng, K., Ling, Q., Zou, Z., and Huang, R.-J.: Evidence of a Large Bias in Rooftop Measurements of Atmospheric Ammonia, ACS Earth Space Chem., 6, 160–164, https://doi.org/10.1021/acsearthspacechem.1c00331, 2022.

Liu, Z., Zhou, M., Chen, Y., Chen, D., Pan, Y., Song, T., Ji, D., Chen, Q., and Zhang, L.: The nonlinear response of fine particulate matter pollution to ammonia emission reductions in North China, Environ. Res. Lett., 16, https://doi.org/10.1088/1748-9326/abdf86, 2021.

Liu, Z., Rieder, H. E., Schmidt, C., Mayer, M., Guo, Y., Winiwarter, W., and Zhang, L.: Optimal reactive nitrogen control pathways identified for cost-effective PM2.5 mitigation in Europe, Nat Commun, 14, 4246, https://doi.org/10.1038/s41467-023-39900-9, 2023.

Pu, W., Ma, Z., Collett Jr, J. L., Guo, H., Lin, W., Cheng, Y., Quan, W., Li, Y., Dong, F., and He, D.: Regional transport and urban emissions are important ammonia contributors in Beijing, China, Environmental Pollution, 265, 115062, https://doi.org/10.1016/j.envpol.2020.115062, 2020.

Wang, Y.: Variation characteristics of atmospheric ammonia concentrations in agricultural areas of North China and Loire, France, Master’s dissertation, Shandong University, Jinan, Shandong, 2021.

Zhang, Y., Tang, A., Wang, D., Wang, Q., Benedict, K., Zhang, L., Liu, D., Li, Y., Collett Jr., J. L., Sun, Y., and Liu, X.: The vertical variability of ammonia in urban Beijing, China, Atmos. Chem. Phys., 18, 16385–16398, https://doi.org/10.5194/acp-18-16385-2018, 2018.

Zhang, Y., Liu, X., Fang, Y., Liu, D., Tang, A., and Collett, J. L.: Atmospheric Ammonia in Beijing during the COVID-19 Outbreak: Concentrations, Sources, and Implications, Environ. Sci. Technol. Lett., 8, 32–38, https://doi.org/10.1021/acs.estlett.0c00756, 2021.

Zhou, M., Liu, H., Peng, L., Qin, Y., Chen, D., Zhang, L., and Mauzerall, D. L.: Environmental benefits and household costs of clean heating options in northern China, Nat Sustain, 5, 329–338, https://doi.org/10.1038/s41893-021-00837-w, 2021.